

Robust Multi-Disciplinary Optimization of Unmanned Entry Capsules

Original

Robust Multi-Disciplinary Optimization of Unmanned Entry Capsules / Ridolfi, Guido; Mooji, E.; Dirkx, D.; Corpino, Sabrina. - ELETTRONICO. - (2012). (Intervento presentato al convegno AIAA Modeling and Simulation Technologies Conference tenutosi a Minneapolis, Minnesota, USA nel 13-16 August 2012) [10.2514/6.2012-5006].

Availability:

This version is available at: 11583/2504390 since:

Publisher:

American Institute of Aeronautics and Astronautics (AIAA)

Published

DOI:10.2514/6.2012-5006

Terms of use:

This article is made available under terms and conditions as specified in the corresponding bibliographic description in the repository

Publisher copyright

(Article begins on next page)

Robust Multi-Disciplinary Optimization of an unmanned Entry Capsule

G. Ridolfi *

*Delft University of Technology, Faculty of Aerospace Engineering,
Politecnico di Torino, Faculty of Aerospace Engineering,*

E. Mooij †

*Delft University of Technology, Faculty of Aerospace Engineering,
Kluyverweg 1, 2629 HS Delft, The Netherlands*

D. Dirkx ‡

*Delft University of Technology, Faculty of Aerospace Engineering,
Kluyverweg 1, 2629 HS Delft, The Netherlands*

S. Corpino §

*Politecnico di Torino, Faculty of Aerospace Engineering,
Corso Duca degli Abruzzi 24, 10126 Torino, Italy.*

I. Introduction

The conceptual design of entry vehicles is commonly done in a number of sequential steps. One usually begins with a generic shape to get a first estimate of the aerodynamic properties and uses a mass-point model for the initial trajectory design. Gradually, more detail is added and the outer shape is changed to accommodate specific mission and/or trajectory requirements.

This shape will largely define the aerothermodynamic characteristics of the vehicle. Since aerothermodynamic challenges, such as vehicle heating, remain one of the most difficult problems in atmospheric re-entry, an exploration of the possible shapes for a vehicle early in the design is advisable. It is advantageous to use a continuous model for the analysis, so that one is not limited to the analysis and comparison of a limited number of shapes, but is instead free to analyze any shape in the design space.¹ With only 5 geometric parameters it is possible to already model the geometry of Apollo-like shapes, as demonstrated later in Section IV.

The internal layout of the subsystems is usually addressed only at a later stage and the designers have to make sure that the mass properties (total mass, location of the center of mass and inertia tensor) meet the requirements. Deviations from these requirements can jeopardize the entire mission, because the loads on the vehicle may change, or the stability and control properties cannot be handled by the Guidance, Navigation, and Control (GNC) system any more. Further, uncertainties related to the entry conditions, environment, the characteristics of the thermal protection system, and the design characteristics and allocation of the equipments on board, pose the multidisciplinary problem to be particularly cumbersome.

In this paper we propose a multidisciplinary, robust optimization approach for the design of unmanned entry capsules in support of the activities of the International Space Station. This problem is handled by minimizing the total mass of the capsules, while maximizing the internal available volume for carrying

*PhD Candidate, g.ridolfi@tudelft.nl, guido.ridolfi@polito.it.

†Assistant Professor, section Astrodynamics and Space Missions, e.mooij@tudelft.nl, Senior Member AIAA.

‡PhD Candidate, section Astrodynamics and Space Missions, d.dirkx@tudelft.nl.

§Assistant Professor, sabrina.corpino@polito.it.

payload. As a third objective, we propose the maximization of the re-usability of the capsules, which can be seen as an attempt to push towards cheaper and more efficient solutions.

The shape, aerothermodynamic, and dynamic mathematical models are adapted from the work of Dirkx and Mooij.² It was demonstrated that the proposed simplified aerodynamic model can predict the aerodynamic forces and moments for ballistic shapes sufficiently well for use at a conceptual design stage. The multidisciplinary design framework is now enriched with a Thermal-Protection System (TPS) model, encompassing re-usable and ablative materials, as well as active cooling mechanisms. This allows for a complete conceptual design of an entry capsule.

Uncertainties of the design variables and environmental factors are integrated into the optimization process to handle *probabilistic* constraints. A probabilistic constraint is a constraint in the design or objective space that shall be satisfied with a pre-defined confidence level. The optimizer thus drives the search of optimal capsules towards those solutions that have the best *expected* performance under uncertain conditions, and that also meet the constraints with a given confidence level, pre-selected by the designer/decision-maker. A sampling-based approach is used to estimate the expected performance of the capsules and to determine the compliance with the probabilistic constraints. For each design point to be evaluated by the optimizer, a set of additional design points is generated around it, according to the joint Probability Density Function (PDF) of the uncertain variables and uncertain environmental factors, and evaluated. To limit the computational effort of the robust optimization, we adopt a double-repository archive maintenance scheme to save all the design-variable combinations computed during the process such that previous design points can be reused at future steps. The double-repository scheme allows to preserve the joint PDF of the input uncertain variables, therefore it is generally applicable with any type of multivariate distribution as input.

This paper is structured as follows. In Section II we provide a brief overview of related work. We then introduce the robust optimization approach and the double-repository archive maintenance scheme in Section III. A short overview of the mathematical models used for the analysis can be found in Section IV. In Section V results are discussed and in Section VI we provide conclusions and recommendations. Two appendix sections, namely Sections VII and VIII provide the thermophysical properties of the materials used for the TPS concepts and the results of the validation of the thermal models respectively.

II. Related work

Although literature on robust (multi-objective) optimization is available, it seems to be still at a pioneering stage. In this section we summarize the main ideas and concepts regarding robust optimization that literature provides and briefly discuss the main contribution of this paper.

II.A. A survey on robust optimization

Jin and Branke⁹ recognize that explicit averaging is the most common approach to robust optimization. This means that the expected value of the performance is taken into account instead of the value computed with a single point in the design space. The expected value is usually computed with Monte-Carlo integration:¹⁴

$$f_{exp}(\bar{x}) = \sum_{i=1}^n \frac{1}{n} f(x_i) \quad (1)$$

The model is indicated by f , while \bar{x} represents a given point in the design space. In this case $x_i = \bar{x} + \delta_i$, where the vector x_i is a set of n sample points in the proximity of \bar{x} generated by the uncertainties in (some of) the design variables distributed according to the joint PDF (δ_i is a realization from the joint PDF).

It is also common that multi-objective algorithms are developed for robust design, where one of the objectives is the expected value and the other is the variance of the performance.^{10,11} In these cases the underlying problem is not multi-objective, and the interest of the designers is to capture the trade-off between robustness and optimality. With true multi-objective problems the approach of optimizing for both the expected value and the variance of each objective will become computationally expensive even with only few objectives, and the final Pareto front would be difficult to interpret.

Constraints in multi-objective optimization engineering problems cannot be neglected, as for instance designing re-entry vehicles, as presented here. With robust-optimization problems the constraints become probabilistic. The reason is that they have to be verified considering a certain envelope of the joint PDF of the design variables and uncertain factors on the design space, and a certain envelope of the joint PDF

of the performance on the objective space. Robust-multiobjective optimization, with constraints, is even less explored in literature. Deb *et al.* propose an integration of reliability-based concepts into evolutionary multi-objective algorithms to deal with this challenging problem.¹³ They consider the utilization of analytical methods to compute the envelope of the joint PDF on the design space that provides a pre-defined confidence level. Then, the constraints are checked given that particular envelope rather than a single point in the design space.

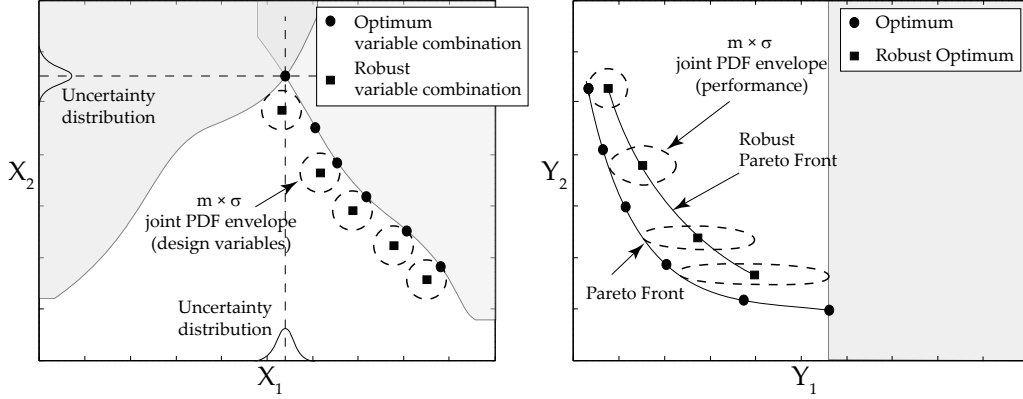


Figure 1: Schematic example of the effect of the probabilistic constraints in the design space (left) and objective space (right). The shaded areas represent the constraints. The dashed lines are the $m \times \sigma$ envelopes of the joint PDF around each specific design point in both the design and objective space.

This means that the constraints have to be satisfied with that specific pre-defined confidence level, $m \times \sigma$. The σ is the standard deviation of the joint PDF, while m is a factor specified by the designers. The analytical approach is feasible when the constraints are in the design space only. When the constraints are also defined in the objective space it is not generally valid anymore. The joint PDF of the performance given the joint PDF of the input may not be trivial to compute analytically, especially in the case of complex non-linear problems, see Figure 1, for instance. Sampling-based approaches may be useful: given a sample in the design space computed with the input joint PDF, the joint PDF of the performance can be estimated using mixture models, for instance, and thus the $m \times \sigma$ envelopes can be estimated as well.^{15,16}

Sampling-based approaches can provide a way of checking probabilistic constraints in the objective space but it is often argued that this advantage may come at the expense of a larger computational cost. This comment is true in general, also for unconstrained robust-optimization only. Indeed, Eq. (1) needs multiple sample points to be computed, and its accuracy increases proportionally to the sample size. Possible solutions proposed to reduce the computational cost of robust-optimization consider the use of variance-reduction techniques for sampling,¹⁷ for instance, or also using *neighborhood* solutions previously computed during the optimizations process.¹⁴ Some other authors also propose repository-based approaches to save these *neighborhood* solutions in such a way to maintain a well-spread distribution in the repository.¹⁹ Paenke *et al.* propose, instead, to use metamodels computed with *neighborhood* solutions and to perform the uncertainty analysis using the metamodel instead of the real model, to save computational time.¹⁸

The main drawback that we see in the direct utilization of *neighborhood* solutions from a repository, is that this approach cannot be used in the presence of specific joint PDF of the input variables. It will work only when the input variables are uniformly distributed (and that it not necessarily always the case) and when there is already a *sufficient* number of sample points on the design space. Without a mechanism for keeping the joint PDF of the uncertain input variables, repository-based robust-optimization cannot be used in general and the advantage obtained by re-using old solutions cannot be exploited.

II.B. Main contributions of this paper

In this paper we propose a double-repository archive maintenance scheme, to allow for re-utilization of old solutions on the design space and at the same time to preserve the joint PDF of the input factors. The scheme allows for the storage of two separate repositories. One repository contains the values of the design variables distributed according to the joint PDF in the design space, this is the *real repository*. The other

repository contains the values of the same design variables in a non-dimensional, uniformly-distributed space, this is the *fictitious repository*. Specific rules for transforming the design points from the real to the fictitious repository, and vice versa, are discussed later in this paper. Whether a certain design point in the real repository is suitable to be reused or not, is determined on the basis of its euclidean distance from the actual design point. The threshold Euclidean distance that allows to determine if two design points are *close enough* is dependent on the joint PDF. A large value of the joint PDF means a large value for the threshold Euclidean distance, and vice versa.

III. Robust-optimization using a Double-Repository Archive Maintenance Scheme

The approach we propose to efficiently incorporate robustness into an optimization process is based on the Unified Sampling Method (USM) presented by the authors in a separate paper.⁶ The main purpose of the USM is to allow for taking all types of uncertainty distributions into account, also epistemic (*i.e.*, where the designer only estimates the probability intervals), exploiting the properties of a *low-discrepancy* sampling technique like the one developed by Sobol'.^{43,44} The basic idea is to uniformly sample in the probability space (between 0 and 1) and then to transform the sample to the actual design-space using the Cumulative Distribution Function (CDF). In Figure 2 we show an example of this procedure considering two independent, uncertain design variables that are distributed according to a Gaussian distribution.

First, the *real* design space (horizontal axis of Figure 2(a)) is subdivided into uniform intervals that are transformed to the probability space using the inverse Gaussian CDF (vertical axis of Figure 2(a)), see the dashed lines of Figure 2(a). This procedure allows us to subdivide the probability space into *bins* with a width proportional to the value of the PDF. We call these *bins* Basic Probability Assignments (BPAs). Then, a uniform sampling is performed on the probability space, as shown in Figure 2(b), obtained with 300 sample points from a Sobol' sequence. The choice of using a Sobol' sequence is due to its characteristic of being a space-filling sampling method that creates a well-distributed set of points. Any other sampling method can be used for this step.

At this point, the CDF is used to transform the design points in the actual design space, as shown in Figure 2(c), see also the full lines of Figure 2(a). As can be seen from Figure 2(c) the sample points are distributed according to a bi-variate Gaussian distribution, as expected. The number of BPAs considered in the double transformation will affect the quality of the final distribution, the more the better. A trade-off exists, however, with the speed of computation of the final joint PDF: using many BPAs will require a higher computational time. According to our experience 30 to 50 BPAs provide already a good balance between the two.

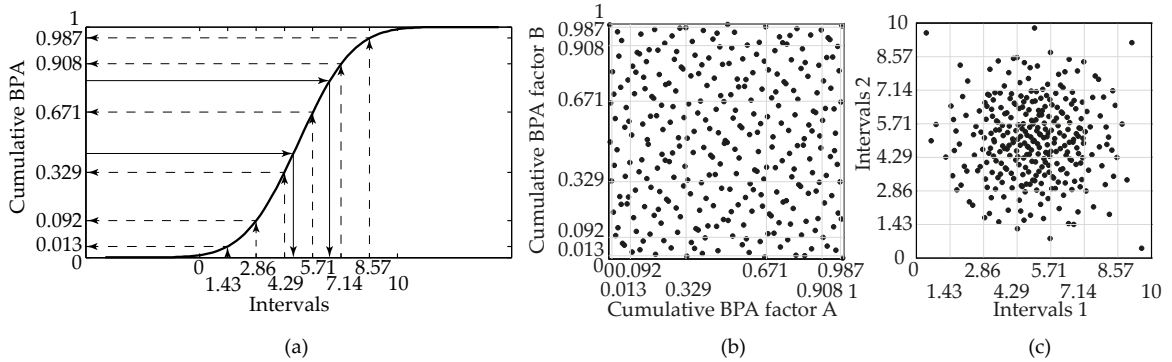


Figure 2: Unified Sampling Method. (a) Cumulative Density Function of a Gaussian distribution of one single variable. (b) Uniform sampling in the probability space of two independent variables. (c) Resulting sampling in the design space.

The double-repository archive maintenance scheme is based on the implementation of the principle explained in Figure 2 during the whole optimization process. To obtain a robust estimation of performance and constraints, by preserving the input joint PDF, a sample as shown in Figure 2(c) needs to be generated

and evaluated for every single design point that the optimizer analyzes. Doing so, Eq. (1) can be evaluated and the probabilistic constraints can be checked as previously discussed. Suppose to begin an optimization process evaluating the first design point. A sample is generated from the joint PDF, then Eq. (1) is computed, constraints are checked for the desired confidence level, and all these points are saved in the repositories, that were empty prior to the beginning of the optimization. The sample points are saved in two distinct repositories. The *real repository* contains the true values of the design points, the points computed as shown in Figure 2(c). The second repository, the *fictitious repository*, contains the design points in a non-dimensional space instead. They are the points computed as shown in Figure 2(b).

When the next design point needs to be evaluated, another sample is generated. At this stage, there are already design points in both repositories. To determine whether some of these pre-existing points can be re-used or not we use the approach schematically shown in Figure 3. Using the non-dimensional version of the new sample, the crowding distances for each point are computed. The crowding distance is a measure used to understand if a pre-existing sample point is *close enough* to the sample point, which has yet to be evaluated. If so, the new sample point is substituted with the pre-existing one, thus saving computational time. In Figure 3(a), the black dots represent the sample points in the non-dimensional space, the radius of each black circle represent the crowding distance of that specific point instead. The crowding distance depends on the BPA to which the sample point belongs. The smaller the BPA, the smaller the crowding distance. In particular, for each BPA the crowding distance is determined as half the minimum distance between two sample points belonging to the same BPA. If there is only one sample point in one BPA, instead the crowding distance is determined as half of the smallest dimension of the BPA itself. This is done because, for events with smaller probability (*i.e.*, toward the edges of Figure 3(a)) the value of the PDF gets more sensitive to small offsets. Once the crowding distance is computed, the sample is transformed and checked against the points in the real repository. In Figure 3(b), the gray points are these belonging to the real repository already, coming from previous evaluations, the black dots are the point belonging to the new sample instead. To preserve the joint PDF, the sample points are checked for each single BPA of the new sample. It is therefore guaranteed that, also in case of replacement of the design points with points already in the repository, in each BPA the number of sample points remains equal to that of the original sample. For instance, in Figure 3(b) Zoom 1, the design point A is substituted by the pre-existing design point 1, because they are in the same BPA and because the distance A-1 is less than the crowding distance of A.

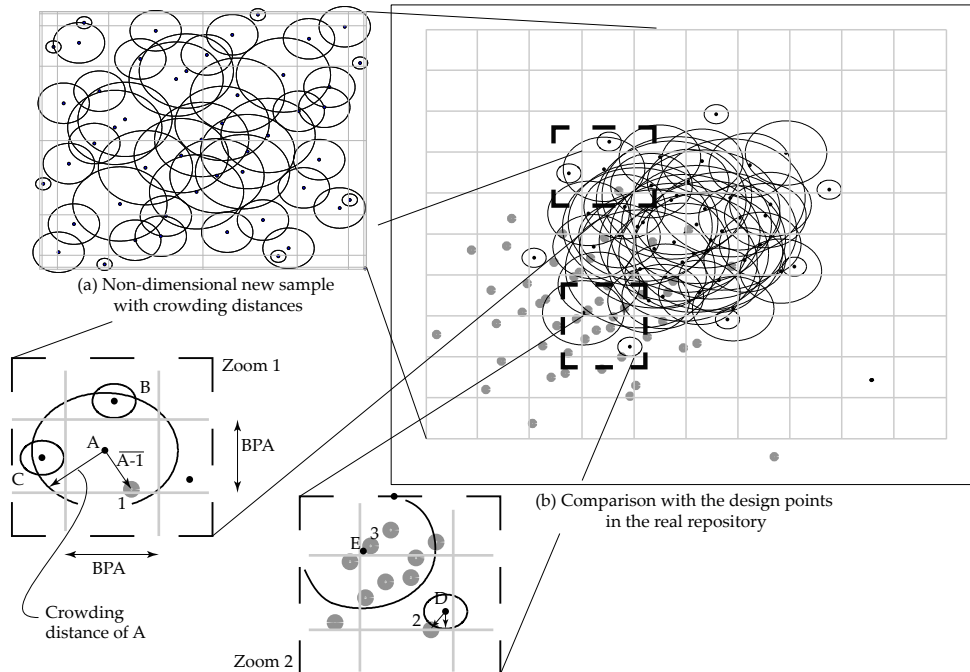


Figure 3: RepositoryExample.

In Figure 3(b) Zoom 2, the design point D cannot be substituted by the pre-existing point 2. Even though they are in the same BPA, their relative distance is larger than the crowding distance of D. Further, even though there are more pre-existing points in that BPA, they are not taken into account because the original BPA only presents one design point, point D. With the same reasoning one can conclude that point E is substituted by point 3 and that no more points are added to that specific BPA.

The final result of the substitution is presented in Figure 4. This represents the true repository with both the samples from the first (gray dots) and the second (black dots) iteration of the optimization process. We would like to mention again that the gray dots have already been evaluated while the black dots not. The squares in Figure 4 are the pre-existing points that substitute some of the points in the new sample, indicated by the cross symbols. In this case it means that 11 simulations are not executed and that Eq. (1) and the constraints are evaluated with the values from the simulations coming from the remaining black dots plus the values from the old simulations (the squares).

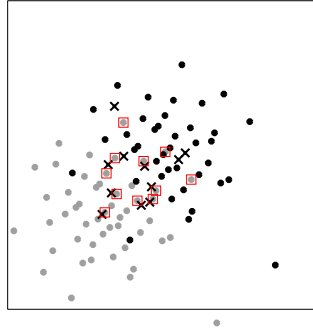


Figure 4: RepositoryExampleFinalStep.

This approach for sampling the design space using the double-repository is called *recursive sampling*. The method is validated with test problems 1 to 4 proposed by Deb *et al.*⁷ The result of the validation is shown in Figure 5. If compared to the results proposed in the original work by Deb *et al.* it can be noticed that there is a perfect match in all the four test cases. These problems are unconstrained and with a uniform distribution of the input uncertain variables. In Figure 5(a) and (b) the values of δ represent the extent of the uncertain boundaries of the design variables. Therefore, $\delta = 0.001$ corresponds to an uncertainty of $\pm 1\%$ around the design variables, for instance. With increasing δ the robust solutions gets more and more distant from the original optimal Pareto front. In Figure 5(c) and (d) the robust Pareto front was obtained with $\delta = 0.03$.

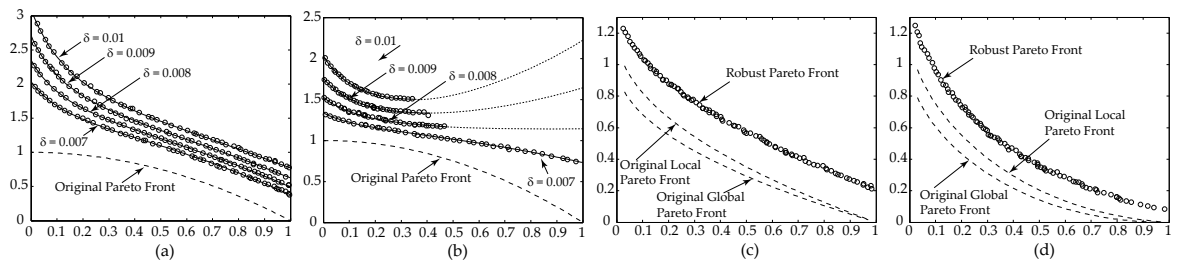


Figure 5: Robust Pareto-front of four test problems with uniform distribution of the uncertain design variables. The symbol δ indicates the width of the uncertain boundaries for the design variables. Graphs (a) and (b) were obtained with the values of δ indicated in the figure. Graphs (c) and (d) were obtained with $\delta = 0.03$.

In Figure 6 it is demonstrated how the recursive sampling allows for a substantial reduction of the number of model evaluations for obtaining the robust Pareto front, if compared to an approach that does not make use of a repository. The lines in Figure 6 represent the number of model evaluations as a function of the number of generations of the optimization algorithm, used for the problem in Figure 5(a). For an approach

without repository, the trend is linear, as shown by the single-dashed line. The continuous lines, instead, represent the trend of the number of model evaluations for varying values of δ . A smaller δ makes the intersection of the design-point sets generated for each single evaluation less likely to happen, thus requiring in general more evaluations (less substitutions) than the cases when δ is larger.

To reduce the computational load even more, also an adaptive selection of the sample points is implemented, following the advice of Luo *et al.*¹² Adaptive selection means that the sample points are considered one-by-one, and that Eq. (1) is computed progressively with one sample point at the time. When the value of Eq. (1) does not change for subsequent executions of the model, then the simulations are stopped for the current sample. Suppose that one decides that the sample for computing the average performance should contain 100 sample points. If, after evaluating 60 sample points the average performance does not change *substantially*, then the remaining 40 sample points are not simulated, saving computational time. The effect of a combined utilization of the recursive sampling and the adaptive selection is also shown in Figure 6. Referring to the results presented in Figure 6, the recursive sampling allows to save approximately 75 % in terms of number of model evaluations, going from 7.5 millions to roughly 2 millions. For moderately computationally expensive models, this difference can turn an infeasible analysis into a feasible one. The Sobol' sampling technique, allows to exploit the adaptive selection at its best reducing of a further 50 % the computational cost of the analysis.

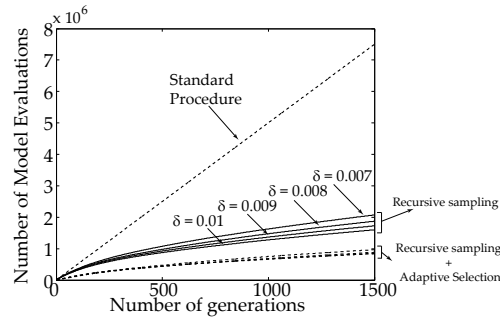


Figure 6: Evolution of the number of model evaluations in the optimization process of the test problem shown in Figure 5(a). The symbol δ indicates the width of the uncertain boundaries.

In Figure 7 we show the performance of the recursive sampling for the robust optimization of a constrained problem. It is a modified version of a test problem proposed by Deb *et al.*,⁸ namely the *DTLZ9*. The original problem is modified by adding the linear constraint in the design space, see the gray area in Figure 7 (right), and an additional constraint in the objective space. The problem is thus formulated as follows:

$$\begin{aligned}
 &\text{Minimize } f_j = \sum_{i=j-1}^j x_i^{0.25}, j = 1, 2 \\
 &\text{Subject to } g_1(x) = f_2^2(x) + f_1^2(x) - 1 \geq 0 \\
 &\quad g_2(x) = f_1 - 0.1 \geq 0 \\
 &\quad g_3(x) = x_1 + x_2 - 0.7 \geq 0 \\
 &\quad 0 \leq x_i \leq 1, \text{ for } i = 1, 2
 \end{aligned} \tag{2}$$

The original problem does not include the constraints g_2 and g_3 , and the original Pareto front is shown as the continuous line in Figure 7(left), the corresponding variable sets are represented by the continuous line in Figure 7(right). When adding the constraints g_2 and g_3 the design and objective space are modified, and the resulting Pareto front and relative variable settings are represented by the diamond symbols in Figure 7. At this point we add uncertainty to the design variables. In particular, we use two normal distributions for the two variables with $\sigma = 0.03$. In Figure 7 the small circles represent the Pareto front (right) and the variable settings (left) obtained with the robust-optimization. The large circles represent the envelopes of the joint PDF that yields a probability of 0.9 in both the design space and objective space. In the objective space, these envelopes are computed using maximum likelihood estimates of the parameters of Gaussian mixture models.^{15,16}

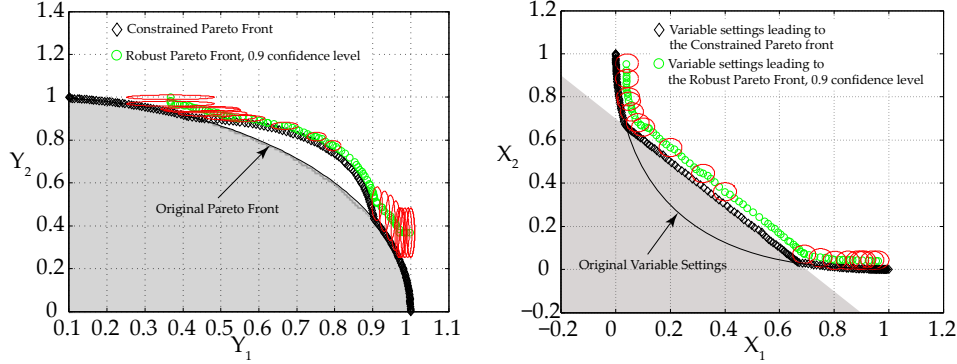


Figure 7: Robust optimization results, problem Eq. (2). The gray areas represent the constraints.

The robust-optimization process pushes the Pareto front away from the non-robust Pareto front in such a way to meet the constraints with a confidence level of 90%. The same phenomenon is also visible in the design space.

IV. Re-entry Capsule Model

In this section we provide a brief overview of the model used for the analysis presented in this paper. In particular we describe the parametrization of the capsule and the Thermal Protection System. Capsule shape generation, aerothermodynamics, flight mechanics and guidance algorithms are adapted from earlier work.^{2,3} For a detailed discussion on these aspects we refer the reader to the original literature.

IV.A. Capsule parametrization

The capsules that will be studied here belong to the family of the Apollo-like capsules. These are axial-symmetric capsules that can be defined by 5 parameters: nose radius, R_N , side radius, R_S , rear part half angle, θ_C , mid radius, R_m , and rear part length, L_C , see Figure 8. The parametrization consists of four matched analytical geometries, namely a sphere segment, a torus segment, a conical frustum and again a spherical segment at the back. Since the shape is axial-symmetric, the entire surface geometry is defined by the cross-section shown in Figure 8.

The shift of the center of mass in the vertical and longitudinal direction are additional variables that may be taken into account in the optimization process. However, the shift in the longitudinal direction does not have a significant effect on the static-stability properties and the dynamic behavior of the capsules.³ Therefore (ΔX_{com}) will not be used as a design parameter.

The following two constraints must hold for the capsule to have a feasible shape:

$$\begin{aligned} R_m &< R_M \\ L_c &< \frac{R_m - R_s (1 - \cos \theta_C)}{\tan \theta_C} \end{aligned} \quad (3)$$

IV.B. Thermal Protection System

The Thermal Protection System (TPS) of a re-entry vehicle is usually very hard to model. Computational Fluid Dynamics (CFD) software allows to approach the problem considering a three-dimensional discretization of the vehicle and the surrounding fluid along the trajectory. In general the temperature profiles obtained using this approach are reliable but usually require a heavy computational load for each single vehicle and each single trajectory. When also non steady-state thermo-chemical reactions are taken into account, with material decomposition, charring, pyrolysis, and mass injection effects, the problem becomes even more complex.

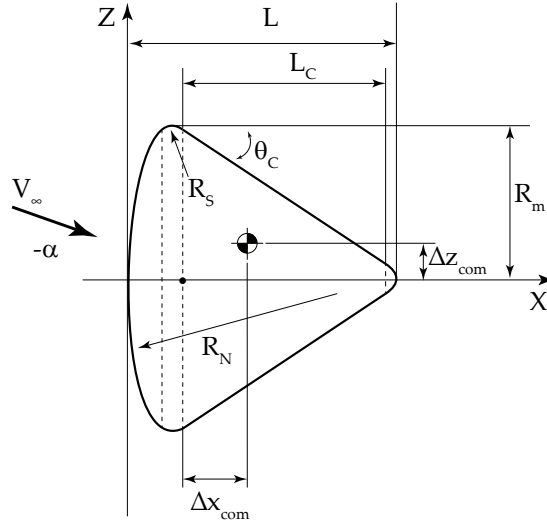


Figure 8: Schematic representation of the geometrical parameters of the capsules. Adapted from.²⁰

In literature, examples can be found to reduce the complexity of modeling re-entry problems to two-dimensional and one-dimensional cases. Chen and Milos, for instance, present a two-dimensional approach to the thermal transfer problem.²⁴ They conclude that such a simplification with respect to the three-dimensional settings could be beneficial for speeding-up the design process of entry vehicles in general, maintaining a certain quality of the solutions. One-dimensional approaches have been investigated more often, especially during the early stages of the Apollo programme. For instance, a complete one-dimensional finite difference model of a charring ablative thermal protection system is provided by Swann et al.^{25, 26}

More recently, general approximated one-dimensional formulations of the heat transfer problem were proposed, demonstrating that at a preliminary design stage these methods can be used for fast analysis while still providing satisfactory results.^{27, 28}

The materials' thermo-physical properties are of crucial importance for the determination of the correct temperatures of the TPS layers, and material consumption in the case of ablation or evaporation/sublimation phenomena. These properties are determined by means of wind-tunnel experiments, but most of the time they are kept classified. Only some data on TPS materials thermo-physical properties can be found.²⁹ If the thermo-physical properties of the materials are not known, or known with large uncertainties, the analysis could have a limited validity, even in the case of a detailed three-dimensional model of the heat-transfer problem.

The main purpose of the TPS model presented in this study is to combine the transient thermal analysis in a large optimization problem with also mission, trajectory, and shape optimization of an entry vehicle. This is done in such a way to substitute the classical heat-flux limits with temperature limits, therefore directly linking the trajectory to the design choices related to the TPS. Due to their reduced execution time, considering that a robust-optimization analysis usually requires a larger number of model evaluations when compared to traditional optimization, a general one-dimensional finite-difference formulation that simulates the stagnation-point conditions and determines the in-depth temperature state along the thickness of the TPS was considered for this analysis. The stagnation point will experience the largest heat-flux and heat-load during the atmospheric entry, thus providing a conservative estimate of the performance of the designed TPS. The material properties and the specific issues related to each material and each solution considered here are described in Section VII.

The one-dimensional finite difference model used in this paper is schematically shown in Figure 9. It is adapted from the formulation presented by Liu and Zhang.³⁰ The TPS is divided into different layers along its axial dimension. Each layer is discretized in isothermal nodes, the distance of which may vary from layer to layer. The thermo-physical properties of the layers are assumed to be isotropic, with a dependency on temperature that will be described case by case in Section VII.

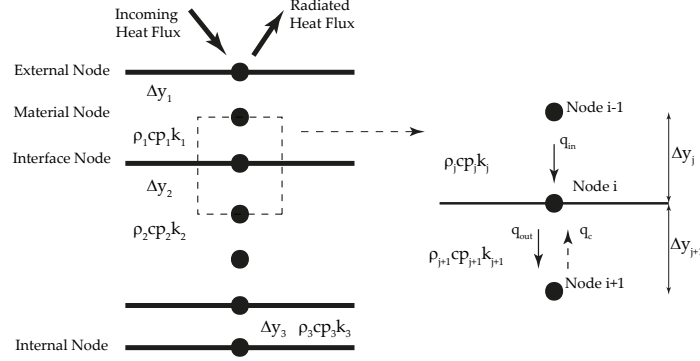


Figure 9: Nodes description of a general finite difference model.³⁰

The nodes are classified in external, material, interface, and internal nodes. The thermal behavior of the external node can be described as follows:

$$\rho c_p A \frac{\partial T}{\partial t} \partial y = \frac{\partial}{\partial y} \left(k A \frac{\partial T}{\partial y} \right) + \dot{q}_{in} - \dot{q}_{out} \quad (4)$$

where ρ indicates the density of the material, c_p the specific heat, A the area, k the thermal conductivity. The term \dot{q}_{in} is the incoming heat flux, while the term \dot{q}_{out} represents in general the radiated heat plus the heat absorbed by transpiration gases in case of ablative material. A finite difference formulation of Eq. (4) is the following:

$$T_1^{t+1} = [\dot{q}_{in} - \dot{q}_{out}] \frac{2\Delta t}{\rho_1 c_{p,1} \Delta y_1} + T_1^t \left(1 - \frac{2k_1 \Delta t}{\rho_1 c_{p,1} \Delta y_1^2} \right) + T_2^t \frac{2k_1 \Delta t}{\rho_1 c_{p,1} \Delta y_1^2} \quad (5)$$

where the symbol t represents the time step, the subscripts 1 and 2 represent the nodes numbers. The symbols Δt and Δy are the temporal and spatial step-size respectively. In the material nodes only conduction and storage of heat are modeled:

$$\rho c_p A \frac{\partial T}{\partial t} \partial y = \frac{\partial}{\partial y} \left(k A \frac{\partial T}{\partial y} \right) \quad (6)$$

Its finite difference formulation can be expressed as follows:

$$T_i^{t+1} = \left(1 - \frac{2k_j \Delta t}{\rho_j c_{p,j} \Delta y_j^2} \right) T_j^t + \frac{k_j \Delta t}{\rho_j c_{p,j} \Delta y_j} (T_{i+1}^t + T_{i-1}^t) \quad (7)$$

Here, j indicates the layer to which the nodes belong. The model of the interface node takes into account an extra flux, \dot{q}_c , that is present in the case of pyrolysis phenomena for ablative materials or heat absorption due to water evaporation, for instance. The assumption is that the pyrolysis manifests on a line rather than on a finite thickness region of the material. For interfaces where no additional heat-flux is present the flux \dot{q}_c is zero.

$$\frac{\partial}{\partial y} \left(-k_j A \frac{\partial T}{\partial y_j} \right) = \dot{q}_c - \frac{\partial}{\partial y} \left(k_{j+1} A \frac{\partial T}{\partial y_{j+1}} \right) \quad (8)$$

Its finite difference formulation can be expressed as follows:

$$\begin{aligned}
T_i^{t+1} = & \frac{2\Delta t}{\rho_j c_{p,j} \Delta y_j + \rho_{j+1} c_{p,j+1} \Delta y_{j+1}} \left(\frac{k_{j+1}}{\Delta y_{j+1}} T_{i+1}^t + \frac{k_j}{\Delta y_j} T_{i-1}^t \right) + \\
& + \left[1 - \frac{2\Delta t}{\rho_j c_{p,j} \Delta y_j + \rho_{j+1} c_{p,j+1} \Delta y_{j+1}} \left(\frac{k_{j+1}}{\Delta y_{j+1}} + \frac{k_j}{\Delta y_j} \right) \right] T_i^t - \\
& - \frac{\dot{q}_c}{A} \frac{2\Delta t}{\rho_j c_{p,j} \Delta y_j + \rho_{j+1} c_{p,j+1} \Delta y_{j+1}}
\end{aligned} \tag{9}$$

At the inner structure nodes, similarly to the material nodes only the heat conduction and heat storage is modeled. A finite difference formulation can be expressed as follows:

$$T_i^{t+1} = \left(1 - \frac{2k_i \Delta t}{\rho_i c_{p,i} \Delta y_i^2} \right) T_i^t + \frac{2k_i \Delta t}{\rho_i c_{p,i} \Delta y_i^2} T_{i-1}^t \tag{10}$$

The finite difference formulation presented here allows for solving the problem with a number of nodes that may vary case by case, and with an explicit forward integration technique. To obtain a faster execution of the thermal transient analysis the results presented in this paper were obtained with an implicit formulation of the problem. It was decided to describe the explicit formulation because it is more direct and it allows for linking it directly to the involved physical phenomena. Having an implicit formulation means that the state at time t depends on previous states but also on the current one. In that way an increase in the time step will keep the integration error low. There are references in literature for solving this type of problems with an implicit formulation.³¹

For the analysis presented in this paper six TPS concepts were developed and implemented. These concepts have been classified in fully re-usable (re-usability index equal to 3), when the nose and rear part are made of re-usable materials. Partially re-usable (re-usability index is equal to 2) when only the nose or the rear part are made of re-usable materials and the other is made of ablative material. The capsule is considered non-reusable (re-usability index is equal to 1) when both the nose and the rear part present ablative solutions. The fully re-usable engineering solutions are metallic uncooled and ZrB₂-SiC, for either the nose or rear part, or both. Further, active cooling mechanisms can be selected by the optimizer for nose and cone. In particular, for the nose direct water-cooling is considered, while enhanced-radiation cooling can be applied to the rear part. The assumptions, and the specific challenges related to each one of these solutions is discussed in Section VII. A validation is provided in Section VIII, instead. Concerning the ablative solutions, ablative carbon-phenolic, phenolic-nylon, and PICA are taken into account.

The re-usability index is also related to the maximum temperature reached during the re-entry of the capsule. After certain temperature thresholds the capsule is considered less reusable if the external temperature gets closer to the limit temperature of the material, see Section VII for the temperature limits of each material.

V. Unmanned Entry Capsules Servicing the ISS

The main focus of this section is to describe the results obtained from the robust-optimization of unmanned entry capsules used as cargo service to the International Space Station. The analysis is carried out using the model described in the previous section and relevant literature, with the robust-optimization method introduced in Section III. The objective is to find trade-offs between minimum mass and maximum volume of the capsules, while maximizing their the re-usability at the same time.

The analysis is also performed by introducing 9 constraints. The external skin temperature of nose and rear part shall not exceed the limits indicated in Section VII for each type of material. The bound-line temperature, which is the innermost temperature of the TPS, shall not exceed 600 K. The capsules shall not exceed a longitudinal load factor of 8 g during the entry phase. The capsules shall be stable and controllable within certain ranges of the angle of attack.² Finally, in the presence of ablative material or water as a cooling mechanism, consumed material should be less than what is actually available, and this applies for both the nose and rear part TPS.

The design parameters and the ranges used for the optimization are presented in Table 1.

The analysis is performed in two steps. First, in Section V.A the results of the optimization are discussed. Then, these results are compared to the results of the robust-optimization in Section V.B.

Design Variables	Intervals	
	Min	Max
Nose radius [m]	1	5
Corner radius [m]	0.001	0.4
Rear part angle [deg] ^a	-60	30
Capsule radius [m] ^a	0.5	5
Capsule length [m]	0.2	3
Z-position CoG [m]	0	0.1
Type of TPS nose [-] ^b	1	6
Thickness Nose [m]	0.0015	0.1
Type of TPS rear part [-] ^c	1	6
Thickness rear part [m]	0.0015	0.1
Initial water-mass nose [Kg]	5	1000
Initial water-mass cone [Kg]	5	1000
Initial flight-path angle [deg]	-6	-2
Initial bank angle [deg]	0	90

Table 1: Reusable capsules design parameters settings.^aConstraints of equation 12 must be considered. ^b1-ZiB2-SiC, 2-Metallic uncooled (heat sink), 3-Phenolic Nylon, 4-Carbon Phenolic, 5-Metallic direct water cooling, 6-PICA. ^c1-ZiB2-SiC, 2-Metallic uncooled (heat sink), 3-Phenolic Nylon, 4-Carbon Phenolic, 5-Metallic enhanced radiation cooling, 6-PICA.

V.A. Optimization

In Figure 10 the Pareto front obtained as a result of the (non robust) optimization process is presented. Three branches can be clearly distinguished. These branches corresponds to fully-reusable capsules, partially reusable capsules, and non-reusable capsules. The optimizer is pushing the solutions toward minimum mass, maximum re-usability and maximum volume, as expected.

The projections of the Pareto-optima solutions on the mass-volume plane show that the performance of the various capsules with different materials are comparable. This means that from the mass-volume trade-off point of view there exists entry conditions and design parameters settings for which, for instance, a capsule with the nose made of ZrB2-SiC and the rear part with metallic enhanced-cooling behaves as a capsule with fully ablative nose and rear part. The capsules in the Pareto front ranges from very small and light to heavy and large ones. Some of the large may simply not be delivered into LEO orbit with current launchers. However, it was decided to set large limits to the geometric variables to see the evolution of the shapes and the engineering solutions on the efficient and robust-efficient Pareto fronts.

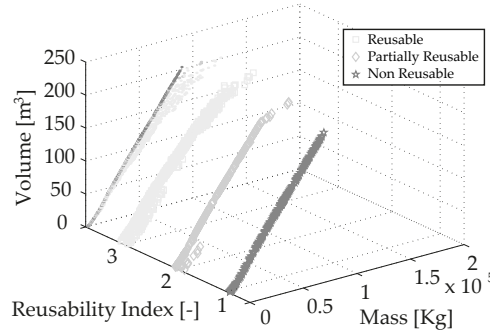


Figure 10: Complete Pareto front, robotic capsules servicing the International Space Station.

In Figure 11 the Pareto front is presented with a focus on the fully-reusable capsules branch of Figure 10.

Almost half of the re-usable capsules have both nose and rear part made of ZrB2-SiC material. However, in the same front there are also capsules with a nose made of ZrB2-SiC and the rear part made of metallic material. Amongst these capsules, the metallic uncooled and the metallic enhanced-cooling concepts are present. Metallic water cooling for the nose is not so common amongst the optimal solutions in the Pareto front. This may be explained from the fact that the tendency is to converge toward large values of nose radius, to maximize the available volume of the capsule. This makes the nose surface to be very large, thus eventually a larger amount of water is needed for a given heat-load to keep the skin cool. A large nose-radius

has two effects. First, it reduces the peak heat-flux on the capsule. At the same time, the total heat load on the nose increases, with the consequent increase of the amount of water required to cool the metallic nose. The increased required water, makes the nose metallic-cooled solution less efficient in terms of mass and volume. In some cases, however, there are conditions for which the peak heat-flux and the heat load are such that a thin metallic external surface cooled by water is more efficient than a thicker metallic skin protecting the capsule with the heat-sink principle, therefore without water cooling from the inside.

As explained earlier, the re-usability index is determined such that it gets worse as the maximum temperature reached by the material gets closer to the limit temperature. Amongst the solutions on the Pareto front of Figure 11, an improvement in the re-usability index causes the capsules to be less efficient in terms of mass and volume. This is what is indicated by the arrow *Decreasing Re-usability* on top of the projection of the Pareto-optima solutions on the mass-volume plane. This effect is more evident as the capsules get larger and heavier. Indeed, a large thickness of nose and rear-part skin, and a large amount of water when applicable, cause the maximum temperature reached at the surface to decrease (so getting farther apart from the limit) but also the mass to increase and the available volume to decrease.

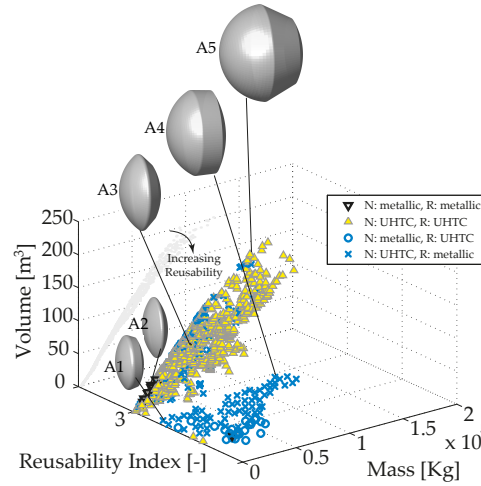


Figure 11: Pareto front with fully re-usable capsules, robotic capsules servicing the International Space Station.

In Figure 11 some of the capsules obtained during the optimization process are illustrated. An expert eye would already recognize the fact that these capsules get worse in terms of aerodynamics and flight-mechanics characteristics as their size increases. However, more quantitative results are summarized in Table 2 and 3. The most relevant trends of the five capsules are also shown in Figures 12 and 13.

	A1	A2	A3	A4	A5
Nose radius [m]	3.64	4.99	4.89	5	5
Corner radius [m]	0.34	0.25	0.33	0.4	0.3
Rear part angle [rad]	-0.34	-1.05	-0.79	-0.06	-0.47
Capsule radius [m]	2.27	3.07	3.88	4.35	4.95
Capsule length [m]	0.6	0.2	0.97	1.95	3
Z-position CoG [m]	0.1	0.065	0.07	0.09	0.08
Type of TPS nose [-]	ZrB2-SiC	Water cooled	ZrB2-SiC	ZrB2-SiC	ZrB2-SiC
Thickness Nose [m]	0.0015	0.0045	0.0015	0.002	0.011
Type of TPS rear part [-]	Metallic Uncooled	Enhanced radiation cooling	Enhanced radiation cooling	Enhanced radiation cooling	ZrB2-SiC
Thickness rear part [m]	0.0087	0.0015	0.0025	0.0015	0.0015
Initial water-mass nose [Kg]	-	730	-	-	-
Initial water-mass cone [Kg]	-	19.5	175	200	-
Initial flight-path angle [deg]	-2.75	-3.95	-2.89	-2	-2.2
Initial bank angle [deg]	84.9	60.73	32.14	20	40

Table 2: Reusable capsules design parameters settings.

	A1	A2	A3	A4	A5
Mass [Kg]	7768	10100	24938	45479	88623
Available volume [m ³]	10	13	52	100	182
Flying range [Km]	1910	1350	1940	3040	2580
Max L/D [-]	0.26	0.17	0.116	0.10	0.03
Max g-load [-]	6.9	7.9	5.2	4.5	7.7
Max heat-flux [MW/m ²]	0.772	0.654	0.672	0.633	1.0
Max temperature nose [K]	2250	577	2150	2160	2300
Max temperature rear part [K]	700	897	900	919	1030
Max temperature bond-line [K]	550	423	547	600	460

Table 3: Reusable capsules summary of the most relevant performance.

The maximum L/D ratio shows a general decreasing trend going from small to larger capsules. This means that the behavior of the capsules gets closer to that of a ballistic entry as their size increases. The larger capsules look much like the Russian *Foton* capsules. For the few capsules with metallic nose, in general the g-load is taken to the limit by the optimizer. This is obtained by having steep trajectories that in turn cause the peak heat-flux to increase and heat-load to decrease. The main driver for the amount of water needed to cool the capsule nose is the heat-load. Therefore a low heat-load will also have an effect on reducing the amount of water to be stored on board and thus reducing the mass of the capsule.

The range that the capsules fly in the atmosphere, from the initial 120 km altitude until Mach 3 is reached, is proportional to the L/D ratio and the flight-path angle. As expected, the capsules show an increased flight range as the trajectory gets shallower (flight-path angle closer to zero) and the L/D ratio increases. The range also indicates, to a certain extent, the heat load that the capsules experience. The larger the range, the larger the time the capsules fly in the atmosphere. This results, in most of the cases, in a larger heat-load on the thermal protection system, see for instance Figure 12(c).

In the case of capsule A2, even if the heat-load is the lowest (the heat-load is determined as the total area under the heat-flux curve) the amount of water needed to take the nose relatively cool is almost 8% of the entire capsule mass. Further, the nose thickness results to be rather large, see Table 2. This means that, for the given design parameters ranges, to obtain a metallic water-cooled capsule nose that meets the temperature constraints there has to be quite a relevant amount of water coupled with a bulky skin that will absorb and store part of the incoming heat. Even if a large amount of water may be required, water-cooling is still a quite effective mechanism for releasing the incoming heat. In Figure 13 the temperature trends of capsule A2, show indeed that even with a peak heat flux that is comparable to that experienced by capsule A3, the water cooling mechanism at the nose allows the temperature to be much lower, thus making the capsule more *reusable*, according to the definition we have given here, by keeping the temperature of the metallic material far from its operating-limit temperature.

The heat-sink mechanism, represented by the metallic uncooled solution, is not as efficient as the others. There are very few capsules on the Pareto front with this solution, and all of them have a heat-sink only on the rear part, where the heat-flux is significantly lower (considered 30% of the stagnation heat-flux). Capsule A1 is representative for these capsules. As presented in Table 2 the thickness of the rear part is relatively large. This makes the thermal protection system in general heavy.

Unlike the other *metallic* solutions, the enhanced-radiation cooling-mechanism for the rear part of the capsules *survives* in the optimization process even for large capsules having a large rear-part exposed surface. This is mostly due to the fact that this unconventional approach to keep a metallic surface cool allows the skin thickness to be very small and still requiring a limited amount of water when compared to the direct water-cooling mechanism. Ultra High Temperature Ceramics, of which ZrB₂-SiC is only one example, performs very well in terms of mass-volume efficiency. A thin skin can provide in general good performance in terms of maximum temperature reached by the material even with very large nose and rear part surfaces.

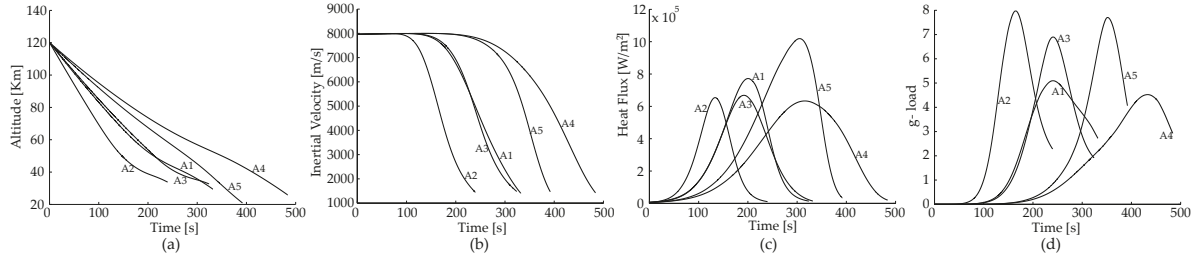


Figure 12: Performance of the capsules A1 to A5.

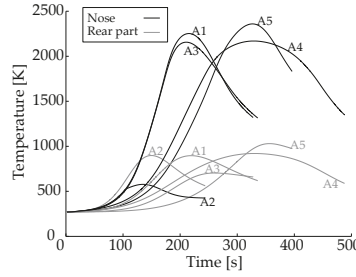


Figure 13: Nose and rear part temperature profiles for the outer skin of the capsules A1 to A5.

V.B. Robust Optimization

In this section the results obtained using the robust-optimization approach with recursive sampling and adaptive selection introduced previously in this paper are described. The results are obtained with a new optimization process. This means that the capsules that will be described will therefore not be just a robust version of the capsules analyzed in the previous section, but rather the most robust-optimal ones that the robust-optimizer was able to provide. The uncertain factors used for the robust optimization are described in Table ???. The objective of this analysis is to illustrate the proposed methodology for robust-optimization. To that end, an attempt was made to select reasonable values for the uncertainties, however these values are for illustration only.

The initial entry velocity is the only uncertain factor that is not also a design variable. This means that its variation is independent from the current position of the design point in the design space. Therefore, the boundaries for the initial velocity are fixed, while the boundaries for the other four uncertain factors are given as a minimum and maximum variation around the current design point. The initial velocity and initial flight-path angle uncertainties are considered to take any possible uncertainty coming from injection conditions into account. The uncertainty related to the position of the center of gravity is meant to account for uncertainties related to manufacturing of the capsules and subsystems placement for subsequent phases of the design cycle. Finally, the uncertainty related to the thickness of nose and rear part thermal protection systems will encompass all these uncertainties related to the accuracy of the 1D thermal model, material properties, and incoming heat flux. These uncertainty boundaries may seem large, however it shall be noted that they represent the 99 percentile of the uncertainty distribution, and that similar uncertainty values can be found in the literature given uncertainty in material density, and thermal properties.³⁹ The capsules obtained with this new optimization process shall be interpreted as these capsules that do not violate the constraints with 99% of confidence and that still present efficient mean performance in terms of mass, volume, and re-usability.

Uncertain Parameters	Intervals		Distribution
	Min	Max	
Z-position CoM [m] ^a	-0.01125	+0.01125	Normal
Thickness Nose [m] ^a	-0.002	+0.002	Normal
Thickness rear part [m] ^a	-0.002	+0.002	Normal
Initial flight-path angle [deg] ^a	-0.5	+0.5	Normal
Initial inertial entry velocity [m/s]	7885	7985	Log-Normal ^b

Table 4: Settings of the uncertain factors.^aIn this case the Min and Max represent the minimum and maximum deviation from the nominal value, which varies with the design point position in the design space. Min and Max are the 0.01 and 0.99 percentile respectively. ^b Min is the 0.99 percentile, Max corresponds to $X = 0$, *i.e.*, the maximum value never exceeded by the log-normal distribution.

The results of the robust-optimization are presented in Figure 14. The complete robust Pareto front resembles the Pareto front of Figure 11, obtained with the non-robust optimization process. This is expected since the uncertain factors do not actually affect the separation between fully reusable, partially reusable, and non reusable thermal protection systems. One general feature that can be observed in Figure 14 is the reduced efficiency that the fully reusable capsules have if compared to the partially reusable capsules, which in turn are less efficient than the non reusable ones. This is observable in the projections of the solutions on the Mass-Volume plane where the branch of the Pareto front with the non-reusable capsules is *higher* than the other two branches. This phenomenon was not present in the original Pareto front where the three branches were aligned on the Mass-Volume plane, besides some trade-offs between mass and re-usability for the fully reusable capsules. This feature can in general be translated in a reduced sensitivity of the ablative materials to the uncertainties of Table ??, that in turn means that non-reusable capsules are more robust and closer to the optimal conditions even in the presence of these type of uncertainties.

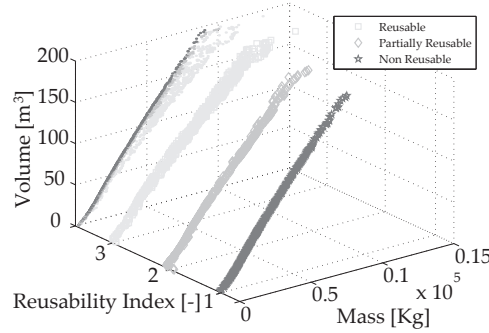


Figure 14: Complete Pareto front obtained with the robust-optimization, robotic capsules servicing the International Space Station.

As done previously, in Figure 15 we focus the attention on the branch of the robust Pareto front with reusable capsules. On the mass-volume plane there is the projection of both the robust Pareto front (gray dots) and the Pareto front of Figure 11 (black dots). As shown in the magnified portion of Figure 15, the optimal-robust solutions are less efficient in terms of performance when compared to the original Pareto-optimal solutions. However, the Pareto-optimal solutions present worse constraint-violation conditions when the uncertainties of Table ?? are taken into account.

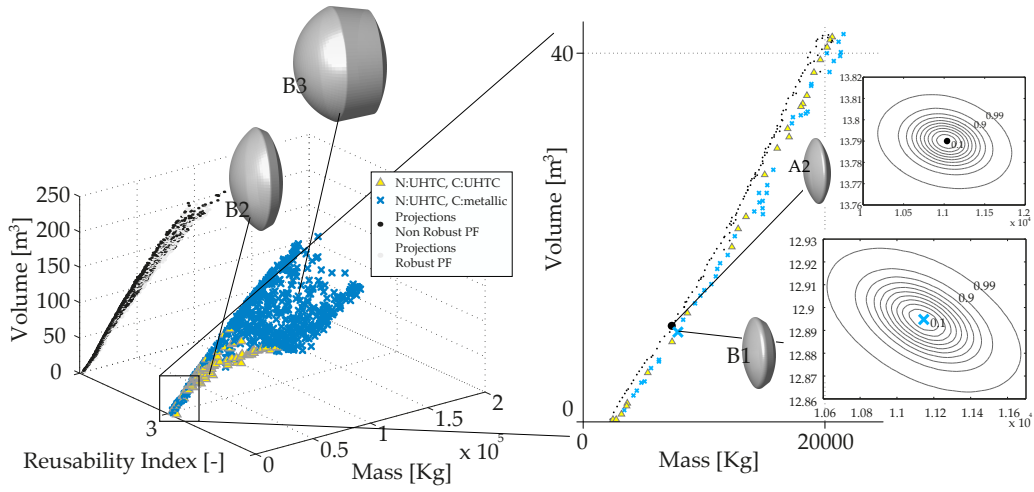


Figure 15: Robust Pareto front with fully re-usable capsules, robotic capsules servicing the International Space Station.

The capsule B1, for instance, presents average performance that is close to the performance of capsule A2, even though it is heavier and with less available volume for payload. However, when subjected to the uncertain conditions described before, capsule B2 proves to be a much better solution than capsule A2. Indeed, as presented in Figure 16 the temperatures reached by the TPS parts are well below the material limits, and also the g-load of the capsule is far from the 8g limit. This is not the case for capsule A2. Under the influence of the uncertain conditions of Table ?? there is the chance that the capsule will not meet the g-load constraint and that the water needed to cool the nose will exceed the actual water within the capsule, as shown in Figure 17.

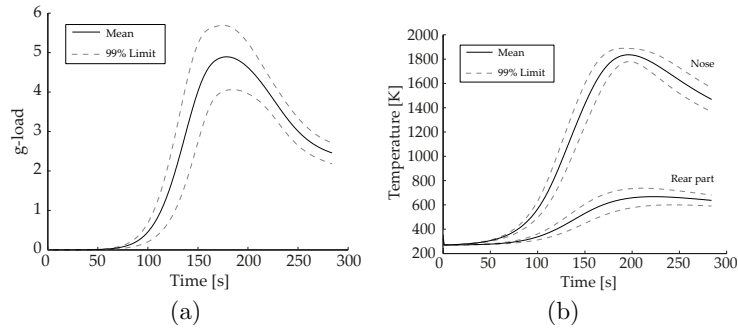


Figure 16: Performance of the capsule B1 under uncertain conditions.

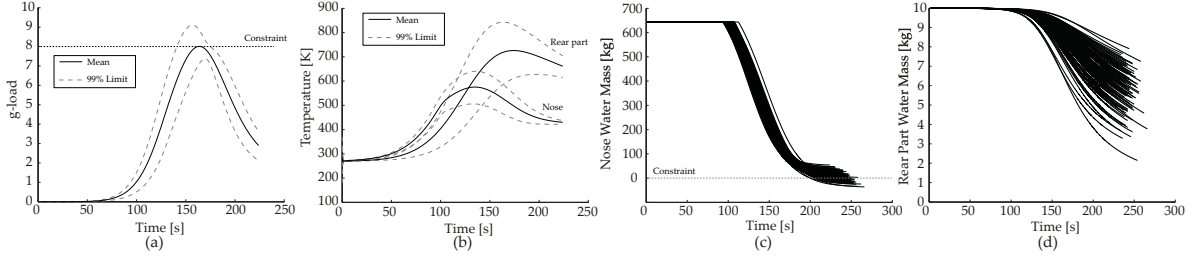


Figure 17: Performance of the capsule A2 under uncertain conditions.

The robust-optimization pushes the robust Pareto front away from the original Pareto front as shown in the zoom in Figure 15, in a similar fashion to the test problems shown before. The effect is that for a given volume, the capsules are heavier. This is driven by the fact that the average thickness of the TPS of both nose and cone gets higher. This effect is actually due to several causes. First of all, in general the trajectories are steeper, meaning that the initial flight-path angle gets lower. This effect, coupled with a reduced shift of the center of mass causes the maximum g-load to decrease as well as the flight range of the capsules. This decreases the heat-load thus providing more robustness in terms of *material consumption*. However, the maximum heat flux increases thus leading to a higher temperature of the external skin. This is true especially for fully re-usable and partially re-usable capsules. Non-reusable capsules, having both nose and rear part of ablative material show a more robust behavior, also in terms of maximum external-skin temperature. The trends introduced here have been quantitatively shown in Figures 18 and 19.

	B1	B2	B3
Nose radius [m]	4.97	4.92	4.96
Corner radius [m]	0.34	0.21	0.29
Rear part angle [rad]	-0.6	-0.47	0.15
Capsule radius [m]	2.7	4.0	4.5
Capsule length [m]	0.54	0.67	2.9
Z-position CoG [m]	0.07	0.082	0.048
Type of TPS nose [-]	ZrB2-SiC	ZrB2-SiC	ZrB2-SiC
Thickness Nose [m]	0.0074	0.002	0.014
Type of TPS rear part [-]	Enhanced radiation cooling	ZrB2-SiC	Enhanced radiation cooling
Thickness rear part [m]	0.002	0.0015	0.0079
Initial water-mass nose [Kg]	-	-	-
Initial water-mass cone [Kg]	80	-	180
Initial flight-path angle [deg]	-3.61	-2.22	-2.58
Initial bank angle [deg]	29	90	14

Table 5: Robust-reusable capsules design parameters settings.

	B1	B2	B3
Mass [Kg] ^a	11150	25550	75275
Available volume [m ³] ^a	12.89	55	142
Flying range [Km] ^a	1704	2337	2274
Max Cl/Cd [-] ^a	0.21	0.12	0.06
Max g-load [-] ^b	5.7	7.9	7.7
Max heat-flux [MW/m ²] ^b	0.71	0.76	1.15
Max temperature nose [K] ^b	1890	2250	2350
Max temperature rear part [K] ^b	737	812	930
Max temperature bond-line [K] ^b	460	560	456

Table 6: Robust-reusable capsules summary of the most relevant performance. ^aValues of the nominal capsule. ^bValues with 99.9% confidence.

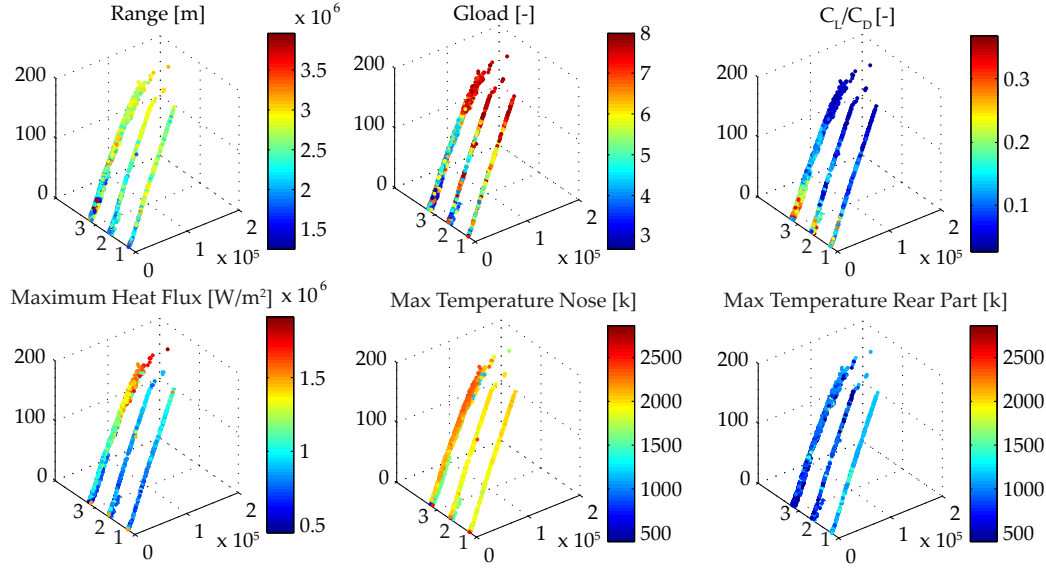


Figure 18: Performance trends on the Pareto front.

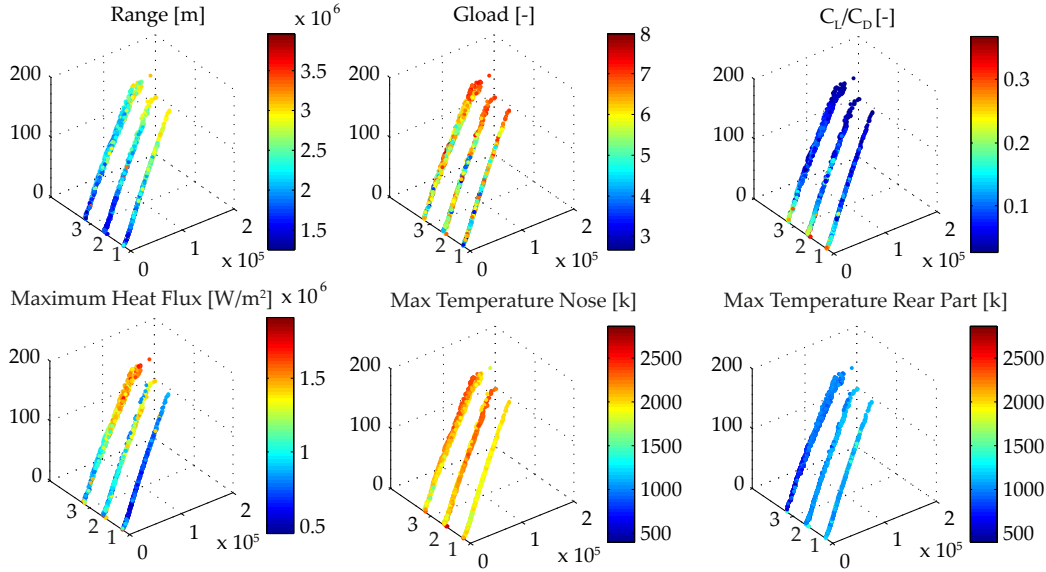


Figure 19: Performance trends on the Robust Pareto front.

VI. Conclusions and recommendations

Robust multi-objective optimization often comes with the price of a large computational cost. This is due to the fact that average performance needs to be computed, therefore many more simulations are needed in the process. In this paper, we introduced a repository-based approach that allows to reduce the computational effort to obtain optimal-robust solutions. At the same time, it allows to keep the joint probability density function of the uncertain factors intact even when sample points are re-used from the repository. This approach to maintain a repository and use it efficiently was used for the study of unmanned re-entry vehicles. The study demonstrates that indeed robust optimization can help in identifying already

optimal solutions that are also robust to uncertainties in the environment, and uncertainties in the design variables themselves. Further, we demonstrated that robust-optimization can also be used to take model uncertainties into account, especially for preliminary design. Specifically for the test case presented here, show that small, fully reusable capsules for unmanned entry from low Earth orbits perform as well as capsules with ablative materials, also under uncertainties. This is also true for large optimal capsules that show, nevertheless, less efficient behavior in the presence of these uncertainties.

VII. Appendix A, material properties

In this section we present the thermo-physical properties of the materials used to obtain the results presented in this paper. All the TPS solutions are obtained with an external skin, an intermediate layer of Saffil insulating material with the thickness of 100 *mm*, and an internal structure of Titanium with the thickness of 3 *mm*. The materials for the insulation layer and the internal structure and their thickness are not part of the optimization. They are equal for all the TPS solutions used in this paper.

VII.A. Metallic TPS solutions

In Table 10 the thermo-physical properties of the PM2000, Saffil insulator, and Titanium are listed. The density of Saffil insulation and Titanium are 96 and 4500 *kg/m*³, respectively. The properties of insulation used here are the effective properties which assume porous insulation material to be isotropic and homogeneous material.³⁰ The density of the PM2000 is 7180 *kg/m*³, its melting point is 1756 *K* while the maximum service temperature is 1623 *K*. The temperature of 1200 *K* is considered the limit for full re-usability of PM2000.

T [K]	C _p [J/g K]	k [W/mK]	T [K]	C _p [J/g K]	k [W/mK]	T [K]	C _p [J/g K]	k [W/mK]
373	0.5	-	273	0.724	0.025	293	0.544	16.33
473	0.48	16.0	373	0.950	0.034	373	0.544	16.33
773	0.61	21.0	473	0.1022	0.043	473	0.628	16.33
1023	0.68	22.0	573	0.1093	0.053	573	0.670	16.75
1273	0.74	25.5	673	0.1139	0.065	673	0.712	17.17
1473	-	28.0	773	0.1172	0.078	773	0.754	18.00
			873	0.1197	0.092	873	0.837	18.00
			973	0.1223	0.108			
			1073	0.1239	0.126			
			1172	0.1252	0.146			
			1273	0.1260	0.167			
			1373	0.1269	0.191			
			1473	0.1273	0.217			

Table 7: Materials thermo-physical properties. PM2000 (left),³⁷ Saffil insulator (center),³⁰ Titanium (right).³⁰

The validation of the thermal model was performed with the material PM1000. PM1000 was used in the original publication, but since it is not in production anymore, we decided to use the PM2000 for the actual robust-optimization process described in this paper.

The density of PM1000 is 8240 *kg/m*³. The following relationships are valid for the thermal conductivity and the specific heat of the PM1000:

$$\begin{aligned}
k_{PM1000} &= 0.025333 \cdot (T - 273.15) + 11 \text{ [W/mK]} \text{ for } 273.15 \text{ K} < T \leq 1023 \text{ K} \\
k_{PM1000} &= 0.026667 \cdot (T - 1023) + 30 \text{ [W/mK]} \text{ for } 1023 \text{ K} < T \leq 1470 \text{ K} \\
Cp_{PM1000} &= 0.408333 \cdot T + 410 \text{ [J/kgK]} \text{ for } 273.15 \text{ K} < T < 1470 \text{ K}
\end{aligned} \tag{11}$$

The metallic TPS solutions also present water as cooling mechanism. The density of the water is 1000 *kg/m*³, its heat of evaporation is 2260000 *J/kg*. The following relationships are valid for the conductivity and specific heat as a function of the temperature, provided in Kelvin:

$$\begin{aligned}
k_{H_2O} &= -0.7676 + 7.536 \cdot 10^{-3}T - 9.825 \cdot 10^{-6}T^2 \text{ [J/mK]} \\
Cp_{H_2O} &= (917.5 - 10.1016 \cdot T + 0.0454134 \cdot T^2 - 9.07517 \cdot 10^{-5}T^3 + 6.8070 \cdot 10^{-8}T^4)/0.018 \text{ [J/kgK]}
\end{aligned} \tag{12}$$

In case of direct water cooling solution, when the temperature of the water reaches the boiling limit, the heat from the skin is absorbed by the water for its evaporation leaving the temperature of the skin at a constant value. Therefore, the water consumption can be expressed as follows:

$$F_{H_2O} = \frac{q_{Aero} - q_{Rad}}{H_{evaporation}} [kg/sm^2] \quad (13)$$

The assumption is that the water is cooling through nucleate boiling. Therefore we consider the temperature of the innermost skin, which is in contact with the water, being at the same temperature of the water itself.

When the enhanced-radiation cooling is adopted, the cooling principle is still based on evaporation but the engineering solution is substantially different, see Figure 20. Water is contained in a porous material, ZAL-15 for instance (a mixture of Alumina 85 % and Silica 15%) that is detached from the external skin. At the interface the heat is transferred through radiation, therefore, equilibrium between the innermost layer of the skin and the ZAL-15 shall be taken into account in the transient model. The water consumption and temperature of the porous material can be computed with the following relationships, where σ indicates the thickness of the porous material and \dot{m} the evaporating water flux:³⁶

$$\Delta T_{H_2O} = \begin{cases} \frac{q_{in}}{\rho_{H_2O} \cdot \sigma \cdot C_{pH_2O}}, & \text{if } T_{H_2O} < T_{boil} \\ 0, & \text{if } T_{H_2O} = T_{boil} \end{cases}$$

$$\dot{m} = \begin{cases} 0, & \text{if } T_{H_2O} < T_{boil} \\ \frac{q_{in}}{H_{evaporation}}, & \text{if } T_{H_2O} = T_{boil} \end{cases} \quad (14)$$

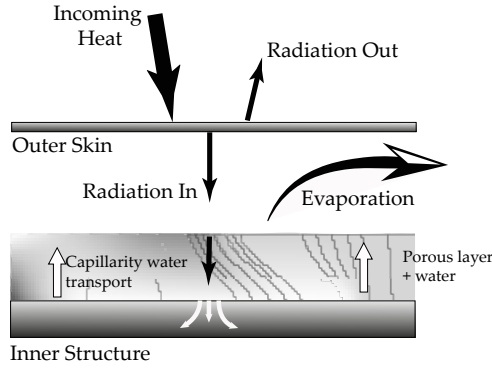


Figure 20: Enhanced Radiation Cooling TPS, schematic representation.

VII.B. Ceramic TPS solutions

The UHTC material used in this paper is the ZrB_2 -SiC. The high-enthalpy test facility of CIRA conducted several experiments on this heat-resistant material, thus some information is available in literature.³⁸ The density of the ZrB_2 -SiC is 5610 kg/m^3 . Its melting temperature is 3020 K , the maximum temperature for single utilization of the material is 2860 K , while it can be reused multiple times is the maximum temperature does not exceed 2300 K . In Table 8 the thermo-physical properties of the ZrB_2 -SiC are presented.

T [K]	C _p [J/g K]	T [K]	k [W/mK]	T [K]	ε
298	0.459	300	103.8	1037	0.775
300	0.462	900	83.07	1169	0.712
400	0.554	1500	76.15	1263	0.72
500	0.603	2100	69.23	1334	0.734
600	0.633	2400	67.50	1485	0.748
700	0.656	-	-	1681	0.724
800	0.673	-	-	1842	0.663
900	0.687	-	-	-	-
1000	0.699	-	-	-	-
1100	0.711	-	-	-	-
1200	0.721	-	-	-	-
1300	0.731	-	-	-	-
1400	0.741	-	-	-	-
1500	0.750	-	-	-	-
1600	0.759	-	-	-	-
1700	0.768	-	-	-	-
1800	0.776	-	-	-	-
1900	0.785	-	-	-	-
2000	0.794	-	-	-	-
2100	0.802	-	-	-	-
2200	0.811	-	-	-	-

Table 8: Thermophysical properties of the ZrB₂-SiC.

VII.C. Ablative TPS solutions

The process related to the ablation is very complex to model. In this paper we adopted a simplified approach to take into account the two main phenomena related to the ablation, *i.e.*, the pyrolysis, at the interface between charred and uncharred material, and the charring at the external interface. These two additional fluxes are taken into account in the model as explained in Section VIII.A regarding the *interface node* and the *external node* respectively. The materials thermo-physical properties presented in this section are derived from the work of Delgado Montes et al.³⁵ concerning the Phenolic Nylon. The Carbon Phenolic properties are adapted from the work of Sutton et al.,³⁴ while the PICA properties are adapted from Parmenter et al.⁴¹ and Tran et al.⁴²

At the outer surface of an ablative TPS several phenomena take place: conduction inwards and radiation outwards of the incoming heat, but also sublimation of the charred material and blockage due to the mass transfer of material in the boundary layer. The *cooling flux* of Eq. (8) and Eq. (9) at the external surface of an ablative TPS is equal to $\dot{m}_c \cdot H_{Subl}$. H_{Subl} is the heat of sublimation, \dot{m}_c is the mass removal rate of the char material:

$$\dot{m}_c = \begin{cases} \frac{1}{H_{Subl}} \left(T_i^t - T_i^{t-1} \cdot \frac{2k_i \Delta t}{\rho C_p \Delta y^2} - T^t - 1_{i+1} \cdot \frac{2k_{i+1} \Delta t}{\rho C_p \Delta y^2} \right) \frac{\rho C_p \Delta y}{2 \Delta t} - q_{Aero} + \sigma \epsilon (T_i^{t-1})^4 & \text{if } T_i^{t-1} \geq T_{Subl} \\ \frac{1}{2} \left(-\frac{(h_e - h_w) K^2 P_w}{q_{Aero} \lambda N^{0.6}} + \sqrt{\left(\frac{(h_e - h_w) K^2 P_w}{q_{Eff} \lambda N^{0.6}} \right)^2 + 4 K^2 P_w C_e} \right) & \text{if } T_i^{t-1} < T_{Subl} \end{cases} \quad (15)$$

The incoming heat flux that should be considered is the effective heat flux, q_{Eff} , which is computed taking into account the blockage effect:

$$q_{Eff} = \alpha q_{rad} + q_{conv} \left(1 - \frac{h_w}{h_e} \right) \left[1 - \left(\frac{0.724 h_e}{q_{conv}} (\alpha_c \dot{m}_c + \alpha_p \dot{m}_p) - 0.13 \left(\frac{h_e}{q_{conv}} \right)^2 (\alpha_c \dot{m}_c + \alpha_p \dot{m}_p)^2 \right) \right] \quad (16)$$

Here q_{rad} and q_{conv} represent the radiative and convective fractions of the incoming heat flux respectively. The symbols h_e and h_w represent the environmental and wall enthalpies, while α_c and α_p represent the transpiration effectiveness of char mass loss and pyrolysis products respectively.

At the interface between charred and uncharred material, the pyrolysis cooling flux is modelled as $\dot{m}_p \cdot H_{Pyro}$, where H_{Pyro} is the heat of pyrolysis, \dot{m}_p is the mass flux of the pyrolysis material:

$$\dot{m}_p = \begin{cases} \left\{ T_i^t - \frac{2\Delta t}{\rho_i C_{p_i} \Delta y_i + \rho_{i+1} C_{p_{i+1}} \Delta y_{i+1}} \left[\frac{k_i}{\Delta y_i} T_{i-1}^t + \frac{k_{i+1}}{\Delta y_{i+1}} T_{i+1}^t \right] - \right. \\ \left. \left[1 - \frac{2\Delta t}{\rho_i C_{p_i} \Delta y_i + \rho_{i+1} C_{p_{i+1}} \Delta y_{i+1}} \left(\frac{k_i}{\Delta y_i} + \frac{k_{i+1}}{\Delta y_{i+1}} \right) \right] T_i^{t-1} \right\} \cdot \frac{-(\rho_i C_{p_i} \Delta y_i + \rho_{i+1} C_{p_{i+1}} \Delta y_{i+1})}{2\Delta t H_{Pyro}} & \text{if } T_i^{t-1} \geq T_{Pyro} \\ 0 & \text{if } T_i^{t-1} < T_{Pyro} \end{cases} \quad (17)$$

The quantities needed to model the ablative TPS, for the three types of ablative materials considered here, are shown in Table 9.

	Phenolic Nylon	Carbon Phenolic	PICA
$\rho_{unchar}[kg/m^3]$	553	1392	266
$\rho_{char}[kg/m^3]$	143	1184	210
$\epsilon [-]$	0.8	0.7	0.9
A $[kg/m^2 \cdot sec \cdot atm]$	4.9E10	4.9E10	4.9E10
B [K]	4.25E4	4.25E4	2.25E4
D $[m^2/s]$	0.85	0.85	0.85
$T_{subl}[K]$	1872	3030	3700
$T_{pyro}[K]$	945	945	1973
$\Delta H_{subl}[J/kg]$	5E7	20.88E6	0.25E9
$\Delta H_{pyro}[J/kg]$	1.28E6	0.465E6	0.5E6
$C_e [-]$	0.23	0.23	0.23
$\lambda [-]$	0.75	0.75	0.75
$h_e [J/kg]$	3.1E6	3.1E6	3.1E6
$\alpha_c [-]$	0.2	0.2	0.2
$\alpha_p [-]$	0.1	0.1	0.1

Table 9: PICA.

The symbols ρ , C_p , and k represent the density, specific heat and conductivity respectively. The symbol ϵ is the emissivity, while A , B , and D represent the reaction rate, activation energy, and diffusion coefficient respectively. P_W is the environmental pressure at the outer edge of the boundary layer, C_e is the oxygen concentration, and λ is the weight of char removed per unit weight of oxygen. The factor K is computed as $Ae^{-B/T}$.

Uncharred			Charred		
T	C_p	k	T	C_p	k
256	0.99	0.561	278	1	0.81
311	1.22	0.639	556	1.38	0.872
367	1.33	0.693	811	1.61	0.935
422	1.39	0.742	1089	1.86	0.977
477	1.45	0.774	1366	2.01	1.128
533	1.51	0.774	1645	2.06	1.189
589	1.56	0.742	1923	2.11	1.502
644	1.62	0.698	2200	2.15	2.065
700	1.68	0.630	2478	2.17	2.790
811	1.80	0.479	2756	2.19	3.502
-	-	-	3030	2.21	4.88
-	-	-	3311	2.24	6.39
-	-	-	3590	2.26	7.38
-	-	-	3867	2.28	9.325

Uncharred			Charred		
T	C_p	k	T	C_p	k
256	0.879	0.0397	0.733	0.0397	
294	0.984	0.0402	0.783	0.0402	
444	1.298	0.0416	1.093	0.0416	
556	1.465	0.0453	1.319	0.0453	
644	1.570	0.0470	1.432	0.0470	
833	1.716	0.0486	1.674	0.0486	
1111	1.863	0.0523	1.842	0.0523	
1389	1.934	0.0560	1.967	0.0560	
1667	1.980	0.0698	2.051	0.0605	
1944	1.988	0.0872	2.093	0.0729	
2222	2.001	0.111	2.11	0.0922	
2778	2.009	0.175	2.135	0.146	
3333	2.009	0.278	2.152	0.223	
-	-	-	-	-	

Table 10: Materials thermo-physical properties. Carbon Phenolic(left), PICA(right). Temperature in [K], C_p in [J/g K], k in [W/mK]

The Phenolic Nylon ablative material presents a specific heat that varies with temperature according to

the following law: $764.04 + 2.812 \cdot T \text{ J/kg} \cdot K$ in the uncharred form. For the charred Phenolic Nylon we considered a constant specific heat equal to $800 \text{ [J/kg} \cdot K]$. Its conductivity is equal to $0.7 + T \cdot 3.457E - 5 \text{ W/mK}$ when uncharred. The charred Phenolyc Nylon presents a conductivity equal to 2 W/mK .

VIII. Appendix B, validation of the thermal models

In this section, we present the results of the validation of the thermal model described in Section , for some of the TPS solutions implemented.

VIII.A. Metallic uncooled TPS, hot structure approach

The background for the verification of the one-dimensional thermal model as described in Section , is provided by Liu and Zhang.³⁰ The TPS in this case is made of an external layer of PM2000 10mm thick. A layer of Saffil insulator with thickness of 50mm is added after, and the internal structure is made of a 5mm Titanium layer. The results of the comparison are presented in Figure 21.

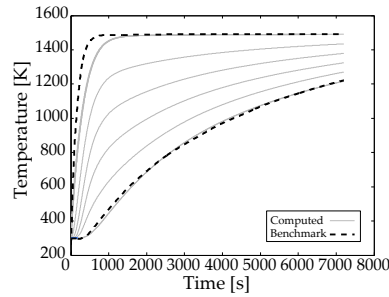


Figure 21: Metallic uncooled TPS. Comparison between benchmark and computed temperatures. Incoming heat-flux 240kW/m^2 .

Once verified that the model is correctly implemented, we can show the validation of the remaining TPS concepts.

VIII.B. Metallic cooled, nucleate boiling and enhanced-radiation cooling approaches

For the validation of the TPS model with cooling mechanisms a capsule with nucleate-boiling at the nose and enhanced-radiation cooling at the rear part is considered. The capsule experiences the heat fluxes presented in Figure 22(a). The computed and the benchmark temperature profiles are very close to each other as evident from Figure 22(b), where also the comparison with the case of a capsule uncooled rear-part is plotted. In Figure 22(c), the water consumed to cool down the nose and the rear part is visualized. The results have been obtained with a PM2000 external skin of 1mm thickness for both nose and rear part. The heat fluxes and the benchmark temperatures are those of the DART capsule, a re-entry test vehicle developed at Delft University of Technology.³⁶

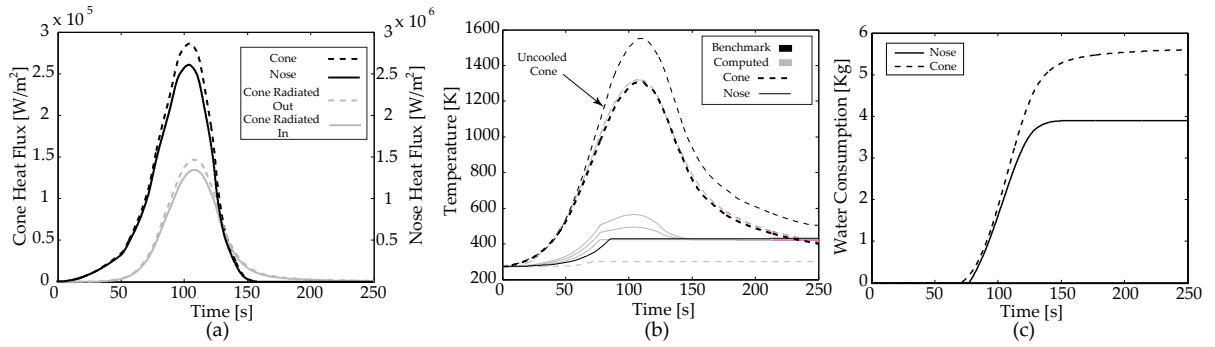


Figure 22: Metallic cooled TPS. (a) Incoming heat fluxes; (b) comparison between benchmark and computed temperatures; (c) Cooling-water consumption.

VIII.C. Ceramic TPS

The performance of the thermal model with the UHTC ZrB₂-SiC TPS are presented in Figure 23 comparing them with the temperature profile obtained for the same material in literature.³²

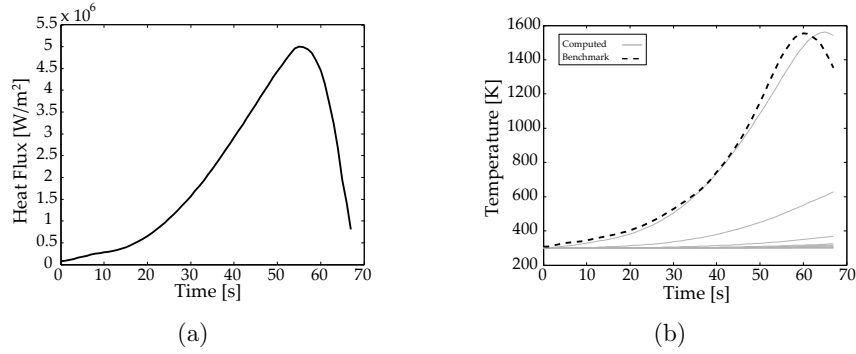


Figure 23: UHTC ZrB₂-SiC TPS. a) Incoming heat flux and (b) comparison between benchmark and computed temperatures.

VIII.D. Phenolic-Nylon ablative material

The convective and radiative heat fluxes used to validate the performance of the thermal model with the Phenolic-Nylon TPS are presented in Figure 24. With an initial thickness of $18mm$, the performance of our model are compared to the results obtained in the original report. The temperature and material recession trends are almost a perfect match, with the only inconvenient of a mild underestimation of the material recession.

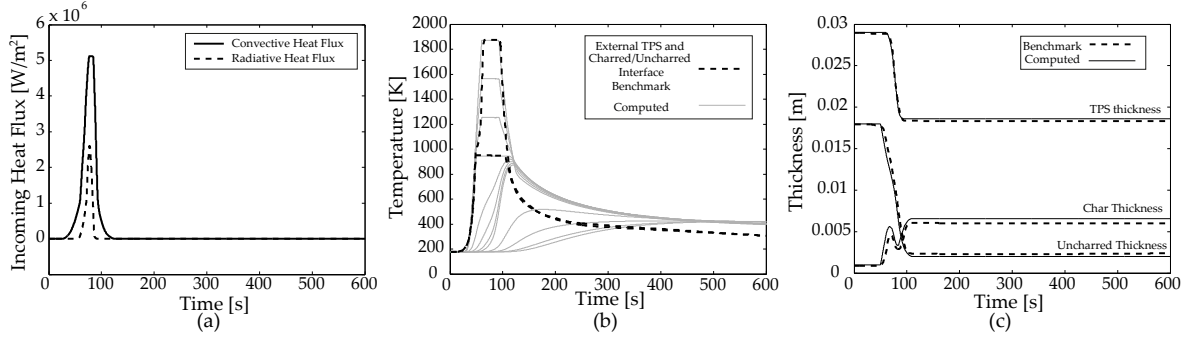


Figure 24: Phenolic-Nylon TPS. (a) Benchmark re-entry capsule heat fluxes on the external surface, (b) comparison between benchmark and computed temperatures, and (c) material recession.

VIII.E. Carbon-Phenolic ablative material

The performance of the thermal model with the Carbon-Phenolic TPS are compared to experimental results obtained with ground-tests with experimental billets of approximately 3.81cm thickness^{??}. The comparison of the experimental temperature data and the computed temperature profile are shown in Figure 25. The temperature data in the high-enthalpy test facility was obtained with an equivalent heat-flux of 1.44W/m^2 , using an atmosphere with an oxygen mass fraction equal to 0.23.

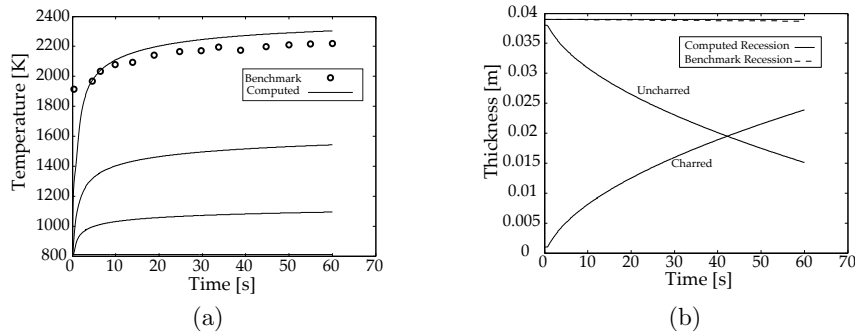


Figure 25: Carbon-Phenolic TPS. Comparison between benchmark and computed (a) temperatures and (b) material recession.

VIII.F. PICA ablative material

For validating the model of the PICA ablative TPS, data from the Stardust Re-entry Capsule (SRC) is used. The SRC entered Earth's atmosphere with an inertial velocity of approximately 12.6km/s . In past planetary missions with high entry heat-loads such as Pioneer-Venus or Galileo, Carbon-phenolic has been used as TPS material. PICA was chosen because it is less dense than Carbon-phenolic and, therefore, has a much lower thermal conductivity with a similar ablation performance.³³

The results obtained with our one-dimensional, stagnation-point, analysis are compared to the results obtained with a much more complete analysis performed in preparation of the Stardust mission.³³ In particular, the results presented in Figure 26 used as benchmark in this study, were obtained by using a two-temperature, non-equilibrium, axisymmetric flow solver, GIANTS2 (Gauss-Seidel Implicit Aerothermodynamic Navier-Stokes Code), coupled with a radiation process model, NOVAR2 (Nonequilibrium Optimized Vectorizable Radiation process model), adapted to incorporate the ablation phenomena. The entry trajectory was then discretized with seven points and laminar flow solutions with coupled radiation were generated with and without ablation. GIANTS/NOVAR and FIAT (Fully Implicit Ablation and Thermal response code) were combined to perform the TPS sizing.³³ As shown in Figure 26 the computed altitude-velocity profile matches the actual altitude-velocity path used to obtain the results in the literature.³³ However, the

peak heat-flux that we are able to compute is equal to $1.1Mw/m^2$, that is lower than the peak heat-flux of $1.2Mw/m^2$ used to compute the benchmark temperature profiles of figure 26.

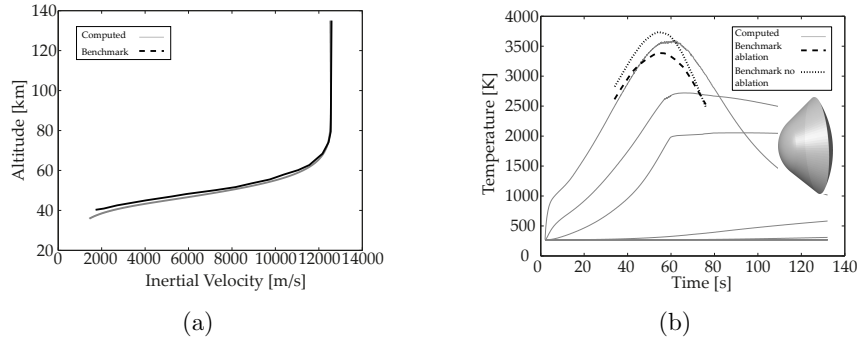


Figure 26: PICA TPS. Comparison between benchmark and computed (a) altitude-velocity profile and (b) external layer temperature trends of the PICA TPS for the Stardust Re-entry Capsule.

References

- ¹Sudmeijer, K. and Mooij, E., "Shape Optimisation for a Small Experimental Re-entry Module," *AIAA/AAAF 11th International Space Planes and Hypersonic Systems and Technology Conference*, 2002.
- ²Dirkx, D. and Mooij, E., "Continuous Aerodynamic Modelling of Entry Shapes", *AIAA Atmospheric Flight Mechanics Conference*, AIAA 2011-6575. 08 - 11 August 2011, Portland, Oregon.
- ³Dirkx, D., "Conceptual Shape Optimization of Entry Vehicles". M.Sc. Thesis, Delft University of Technology, 2011.
- ⁴Ridolfi, G., Mooij, E., and Chiesa, S., "A Modelling Framework for the Concurrent Design of Complex Space Systems". AIAA GNC conference proceedings. August 2010, Toronto. AIAA 2010-7782
- ⁵Ridolfi, G., Mooij, E., and Corpino, S., "A System Engineering Tool for the Design of Satellite Subsystems". AIAA GNC conference proceedings. August 2009, Chicago. AIAA 2009 6037
- ⁶Ridolfi, G., Mooij, E., Corpino, S., "Complex - systems design methodology for Systems-Engineering collaborative environment". *Systems Engineering Theory and applications*, ISBN 979-953-307-410-7. To be published in February 2012, by In Tech.
- ⁷Deb, K. and Gupta, H., "Searching for Robust-Optimal Solutions in Multi-Objective Optimization", C.A. Coello Coello *et al.* (Eds.): EMO 2005, LNCS 3410, pp. 150-164. Springer-Verlag Berlin Heidelberg 2005.
- ⁸Deb, K., Thiele, L., Laumanns, M. and Zitzler, E., "Scalable Test Problems for Evolutionary Multi-Objective Optimization". Computer Engineering and Networks Laboratory (TIK), Swiss Federal Institute of Technology (ETH), 2001.
- ⁹Jin, Yaochu, and Branke, J., Evolutionary Optimization in Uncertain Environments - A Survey. *IEEE Transactions on Evolutionary Computation*, Vol. 9, No. 3, June 2005.
- ¹⁰Hassan, R., Crossley, W., Spacecraft Reliability-Based Design Optimization Under Uncertainty Including Discrete Variables. *Journal of Spacecraft and Rockets*. Vol. 45, No. 2, March-April 2008
- ¹¹Luo, B., and Zheng, J., A New Methodology for Searching Robust Pareto Optimal Solutions with MOEAs. *IEEE Congress on Evolutionary Computation*, 2008.
- ¹²Luo, B., and Zheng, J., Efficient MOEAs with an Adaptive Sampling Technique in Searching Robust Optimal Solutions. *World Congress on Intelligent Control and Automation* June 25 - 27, 2008, Chongqing, China.
- ¹³Deb, K., Gupta, S., Daum, D., Branke, J., Mall, A.K., Padmanabhan. Reliability-Based Optimization Using Evolutionary Algorithms. *IEEE Transactions on Evolutionary Computation*. Vol. 13, No. 5, October 2009.
- ¹⁴Branke, J., Creating robust solutions by means of an evolutionary algorithm. *Parallel problem solving for Nature-PPSN V*, pp. 119-128, 1998.
- ¹⁵McLachlan, G., and D. Peel. *Finite Mixture Models*. Hoboken, NJ: John Wiley & Sons, Inc., 2000
- ¹⁶Marin, J.M., Mengersen, K. and Robert, C.P. Bayesian modelling and inference on mixtures of distributions. *Handbook of Statistics* 25, D. Dey and C.R. Rao (eds). Elsevier-Sciences.
- ¹⁷Loughlin, D.H., and Ranjithan, S.R., Chance-constrained genetic algorithms. *Genetic and Evolutionary Computation Conference*, pp. 369-376, 1999.
- ¹⁸Paenke, I., Branke, J., and Jin, Y., Efficient Search for Robust Solutions by Means of Evolutionary Algorithms and Fitness Approximation. *IEEE Transactions on Evolutionary Computation*, Vol. 10, No. 4, August 2006.
- ¹⁹Kruisselbrink, J., Emmerich, M., and Back, T., An Archive Maintenance Scheme for Finding Robust Solutions. R. Shaefer *et al.* (eds.): PPSN XI, Part I, LNCS 6238, pp. 214-223, 2010. Springer-Verlag Berlin.
- ²⁰Hirschel, E.H. and Weiland, C., "Selected Aerothermodynamic Design Problems of Hypersonic Flight Vehicles". Springer - AIAA. Berlin, 2009.
- ²¹NOAA/NASA, US Standard Atmosphere, 1976, Tech. rep., U.S. Government Printing office, 1976.

- ²²Mooij, E. The motion of a vehicle in a planetary atmosphere. Series 08, Astrodynamics and Satellite Systems, Delft University Press, 1994.
- ²³Shen, Z. and Lu, P., "Onboard generation of three-dimensional constrained entry trajectories". Journal of Guidance, Control, and Dynamics. Vol 26, No.1, 2003.
- ²⁴Chen, Y.K. and Milos, F.S., Thermal response modeling system for a Mars sample return vehicle. Thermal and Fluids analysis workshop, 2001. Thermal Protection Materials and Systems Branch NASA Ames Research Center, MS 234-1 Moffett Field, CA 94035-1000.
- ²⁵Swann, R.T. and Pittmann, C.M. Numerical analysis of the transient response of advanced thermal protection systems. NASA TN D-1370, 1962, Langley Research Center, Hampton, VA.
- ²⁶Swann, R.T., Pittmann, C.M. and Smith, J.C. One-dimensional numerical analysis of the transient response of thermal protection systems. NASA TN D-2976, 1965, Langley Research Center, Hampton, VA.
- ²⁷Ferraiuolo, M. and Manca, O. A New Methodology to Preliminary Design Structural Components of Re-Entry and Hypersonic Vehicles. Book Chapter of Wind Tunnels and Experimental Fluid Dynamics Research, No. 19, pp 409-426, 2011. In Tech publisher, ISBN: 978-953-307-623-2
- ²⁸Martinelli, S.K. and Braun, R.D. Centerline Heating Methodology for Use in Preliminary Design Studies. IEEEAC paper 1322, 2011. ISBN: 978-1-4244-7351-9/11
- ²⁹Williams, S.D. and Curry, D.M. Thermal protection materials. Thermophysical property data. NASA RP-1289, 1992.
- ³⁰Liu, S. and Zhang, B. Effects of active cooling on the metal thermal protection system. Aerospace Science and Technology, No. 15, pp 526 - 533, 2011. DOI:10.1016/j.ast.2010.08.001
- ³¹Press, W.H., Teukolsky, S.A., Vetterling, W.T., Flannery, B.P. Numerical Recipes. The Art of Scientific Computing. Cambridge University Press, New York, Third Edition. ISBN-13 978-0-511-33555-6
- ³²Savino, R., De Stefano Fumo, M., Paterna, D., Serpico, M. Aerothermodynamic study of UHTC-based thermal protection systems. Aerospace Science and Technology 9 (2005) 151160. DOI:10.1016/j.ast.2004.12.003
- ³³Olynick, D., Ghent, Y.K., and Tauber, M.E. Forebody TPS Sizing with Radiation and Ablation for the Stardust Sample Return Capsule. Thermophysics Conference, 32nd, Atlanta, GA, June 23-25, 1997. AIAA-1997-2474
- ³⁴Sutton, K., An Experimental Study of a Carbon-Phenolic Ablation Material. NASA TN D-5930. NASA Langley Research Center, Hampton, Va.
- ³⁵Delgado Montes, I., Study on Aerocapture Guidance and Navigation, Analysis of a Charring Ablator Thermal Protection System. GMVSA 2067/88. Grupo de Mecanica del Vuelo, S.A.
- ³⁶Buursink, J., On the Development of a Cooled Metallic Thermal Protection System for Spacecraft. Ph.D. dissertation, Delft University of Technology, 2005. ISBN-10 9056230808.
- ³⁷Schwarzkopf Plansee PM2000 data sheet. URL: <http://www.matweb.com>, last visited February 2012.
- ³⁸Francese, A., Numerical and experimental study of UHTC materials for atmospheric re-entry. PhD dissertation, Universit degli studi di Napoli Federico II.
- ³⁹Mazzaracchio, A., Marchetti, M., A probabilistic sizing tool and Monte Carlo analysis for entry vehicle ablative thermal protection systems. Acta Astronautica 66, pp. 821-835, 2010.
- ⁴⁰Milanese, M., Vicino, A., Optimal Estimation Theory for Dynamic Systems with Set Membership Uncertainty: An Overview. Bounding approaches to Systems Identification. Plenum Press, New York, 1996.
- ⁴¹Parmenter, K.E., Shuman, K., Milstein, F., Szalai, C.E., Tran, H.K., Rasky, D.J., Compressive Response of Lightweight Ceramic Ablators: Phenolic Impregnated Carbon Ablator. Journal of Spacecraft and Rockets, Vol. 38, No. 2, March/April 2001.
- ⁴²Tran, H.K., Johnson, C.E., Rasky, D.J., Hui, F.C.L., Hsu, M., Chen, T., Chen, Y.K., Paragas, D., Kobayashi, L., Phenolic Impregnated Carbon Ablators (PICA) as Thermal Protection Systems for Discovery Missions. NASA Technical Memorandum 110440, April 1997.
- ⁴³Sobol, I.M., On the Systematic Search in a Hypercube, SIAM Journal on Numerical Analysis, No. 5, Vol. 16, pp. 790-793, 1979.
- ⁴⁴Antonov, I.A. and Saleev, V.M., An Economic Method of Computing lpt Sequences, USSR Computational Mathematics and Mathematical Physics, No. 1, Vol. 19, pp. 252-256, 1979.